A database and meta-analysis on the performance of exploding pusher implosions conducted at OMEGA

P. J. Adrian,[1,*] M. Gatu Johnson,[2] N. V. Kabadi,[3] G. D. Sutcliffe,[4] and J. A. Frenje[2]

[1] *Los Alamos National Laboratory, Los Alamos, New Mexico 87545, USA*
[2] *Plasma Science and Fusion Center: MIT, Cambridge, MA 02139*
[3] *Laboratory for Laser Energetics, University of Rochester, Rochester, New York 14623, USA*
[4] *Lawrence Livermore National Laboratory, Livermore, CA 94550*

(Dated: March 6, 2025)

A database of 222 exploding-pusher implosions conducted at the OMEGA laser facility is presented. The data-set consists of glass-shell capsules filled with varying pressures of D_2, T_2, and ^{3}He, which were imploded using square laser pulses with intensities ranging from 1-10 $\times$ 10^{14} W/cm^2. The database includes measurements of bang-times, ion temperatures, and yields from the DD, D^{3}He, and DT fusion reactions. A semi-analytic exploding pusher model is introduced, which effectively captures the observed trends in the data. This model predicts that the measurements scale according to a power-law relation based on the initial capsule and laser conditions. A generalized power-law scaling relation is directly fit to each data set, providing a useful interpolation of the entire database. Overall, the database provides a valuable resource to estimating bang times, temperatures, and yields for the design of future experiments. Additionally, it provides a diverse set of data for validating more advanced implosion physics models.

I. INTRODUCTION

Exploding pusher platforms are studied for the unique plasma conditions they generate at the OMEGA Laser Facility [1] and at the National Ignition Facility (NIF) [2]. Exploding pushers are capsules with low-mass ablators, which are imploded to generate plasmas heated by a spherically converging shock that disassembles rapidly [3]. Both OMEGA and NIF employ exploding pushers, driven by either direct or indirect drive [4], for a variety of purposes. The high yields and low areal densities makes these experiments ideal for the calibration of neutron activation diagnostics for areal density measurements [5–7]. Additionally, significant efforts are underway to utilize exploding pushers as neutron sources to take advantage of the large neutron fluxes and the ability to place witness samples close to the source [8, 9]. Exploding pushers are also used in studies of stellar nucleosynthesis reactions because the large volumes and high temperatures enable the detection of low-cross section fusion reactions, such as the ^{3}He-^{3}He reaction [10–12]. Furthermore, exploding pushers are optimized for fundamental studies of high energy density physics (HEDP) to study different fundamental process such as charge particle stopping [13, 14] and diffusion [15–17]. Overall, the exploding pusher is an economical and versatile experimental platform with unique characteristics broadly utilized by HEDP community.

This paper presents a database of 222 glass-shelled exploding-pusher implosions conducted at the OMEGA Laser Facility over the past decade. The data set includes the initial conditions of the capsule and laser pulse, as well as, the nuclear data from the D+D, D+^{3}He, and D+T fusion reactions. A simplified exploding-pusher model is presented, providing physics insight into the temperature and yield scaling observed in these experiments. Based on this model empirical scaling models are constructed to relate the initial conditions of the capsule to the nuclear measurements. These scaling expressions are intended to assist and inform the design and execution of future experiments.

This paper is organized as follows. Section II presents details of the database as well as the parameters space covered by the capsule and laser initial conditions. Section III details a semi-analytic model for describing the temperature and density reached by an exploding pusher at stagnation. Section IV presents a simple scaling model fit the the nuclear measurements which provides efficient interpolations of the database that can be used to aid the design of future experiments. Section V discusses the observed yields scaling in the context of previous work. Lastly, Section VI concludes and highlights potential future additions to the data set, as well as applications.

II. DATABASE

The database consists of 222 experiments conducted between 2012 and 2020. The focus is exclusively on glass capsules imploded with a square

* Author to whom correspondence should be addressed:pjadrian@lanl.gov

laser pulses and filled with combinations of D_2, T_2 and ^{3}He gas at ambient conditions. The shot numbers and initial conditions are included in a data sheet provided in the Supplemental Material. The capsule specifications are the shell outer radius (R_0), shell thickness (ΔR), total fill density (ρ_0), and the average 4π non-uniformity of the shell (δR). The laser is characterized by the total energy (E_L) and the pulse duration (Δt).

Figure 1 displays the parameter space distribution to help visualize the range of conditions covered by the data set. A large fraction of the capsules are R_0= 430 μm, as this is approximately the beam-spot size on capsule. However, targets up-to 1150 μm are included. The data set primarily consists of targets with ΔR = 2-4 μm and the non-uniformity of the shell is generally kept to variations well below δR = 0.5 μm. The targets are filled with ρ_0 in the range of 0.1 to 3 mg/cc and a wide combination of D, T, and ^{3}He fill fractions. The laser energies vary in the range of 5 to 30 kJ, resulting in intensities on capsule from 1-10 $\times$ 10^{14} W/cm^2. The square pulse widths are in discrete increments of 0.6, 0.8 1.0, and 2.0 ns.

The data set includes the corresponding fusion yields (Y_{DT}, Y_{DD}, Y_{D3He}), ion temperatures (T_{DT}, T_{DD}) , and bang times (t_{BT}) for each experiment. Neutron-time of flight detectors at OMEGA were used to measure Y_{DT}, Y_{DD}, T_{DT}, and T_{DD} [18]. Generally the neutron yields are accurate to 5% and the error on the temperatures is $\pm$ 0.5 keV. Wedge range filters were used to measure Y_{D3He}, which is generally accurate to 10% [19]. The Neutron Temporal Diagnostic measured t_{BT} from the DD or DT neutron emission history with absolute uncertainty of $\pm$50 ps [20]. The data for each shot, when available, is given in the data sheet provided in the Supplemental Material.

The database includes previously published experiments. Early experiments exploring kinetic effects in ICF implosions by Rosenberg *et al.* are included which utilized D^{3}He exploding pushers filled at a variety of ρ_0 [21, 22]. A set of DT exploding pushers published by Kabadi *et al.* explored differences in the DD and DT temperatures due to thermal decoupling of the ion species by primarily changing ρ_0 [23]. In addition, the data base includes high yield DT implosions by Mannion *et al.* [24] who studied the impact of kinetic effects on DT neutron spectra and Aguirre [25] who used the large neutron fluxes for radiation damage effects testing. Experiments utilizing DT^{3}He implosions for stellar nucleosythesis studies [26, 27] and development of the tri-particle back-lighter [28] are included. Experiments which optimized Y_{DT}, Y_{DD} and Y_{D^3He} to be measured multiple reaction histories [16, 29, 30] are also included. Lastly, the data base includes published experiments pertaining to the study of ion stopping powers [14]. There are also experiments included in this data base that have either supported previous published experiments but are not published previously.

III. EXPLODING PUSHER MODEL

The experiments in this database produced ion temperatures ranging from 5 keV to 20 keV and nuclear yields spanning six orders of magnitude. Developing a simplified model to capture the trends observed in this data set is highly desirable. Rosen and Nuckolls previously developed a semi-analytic model for predicting the performance of exploding-pusher targets at the Shiva laser [3]. This model divided the exploding pusher implosion into two distinct phases. The first phase applied linear shock theory to the early stages of the implosion to compute the plasma conditions generated by the strong shock launched by the collapsing shell. The second phase amplifies the plasma conditions computed in the shock phase by adiabatic compression. This work builds on the core concept proposed by Rosen, however, significant modifications were made to describe the performance observed in the OMEGA data set. The key modification was the direct modeling of the shell and shock trajectory when computing the plasma conditions at both phases. This section presents the governing equations of motion governing the shell and the resulting shock wave launched into the gas. The linear shock phase is presented followed by the adiabatic compression phase. The new model is used to predict the DT measurements and compares reasonably well with the data. Finally, the model motivates the idea that the measurements can be described by power-law functions of the initial capsule and laser conditions.

A. Shell Equations of Motion

The motion of the shell is determined by the laser-matter coupling, which drives the shell inward and determines the strength of the strong shock launched into the ambient gas. The shock position and velocity are two critical parameters for modeling the plasma conditions generated at peak compression. The equations for the evolution of the shell radius (R), shell velocity (V), and shell mass (M) are given

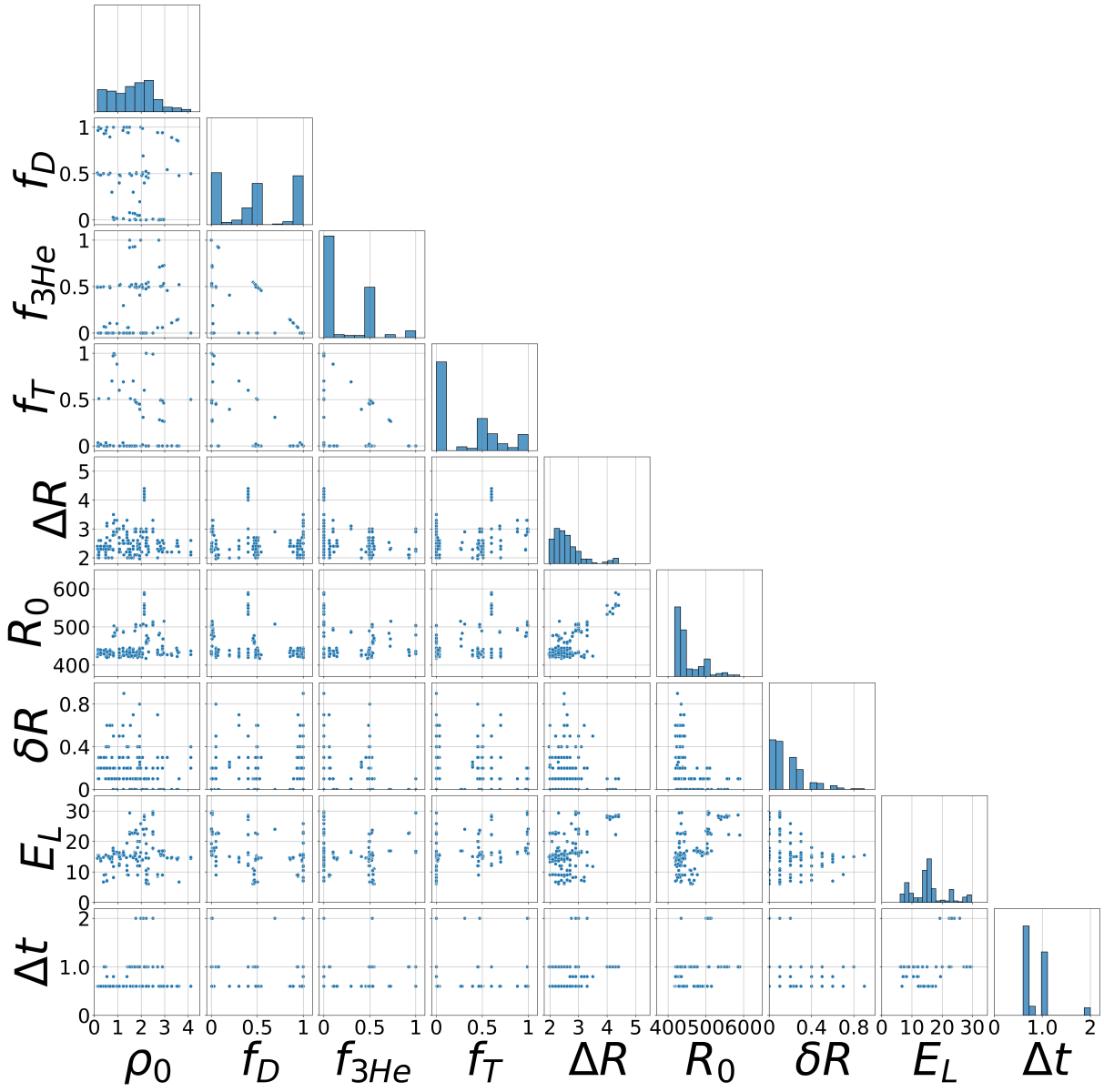

FIG. 1. Parameter space covered by the data set. The main diagonal plots show histograms of the distribution of variables. The off-diagonal plot show bi-variate distribution of each parameter to illustrate the combinations of parameters probed the the data set. The variables and their units are the initial fill density (ρ_0 [mg/cm^3]), the initial fill fraction of Deuterium, Helium-3, and Tritium (f_D, f_{3He}, f_T), the shell thickness (ΔR [μm]), the outer radius (R_0 [μm]), the 4π average wall variation (δR [μm]), the laser energy (E_L [kJ]), and the pulse width (Δt [ns]).

by

$$\frac{d\hat{R}}{d\hat{t}} = -\hat{V} \tag{1}$$

$$\frac{d\hat{V}}{d\hat{t}} = -\frac{\hat{R}^2}{\hat{M}} \tag{2}$$

$$\frac{d\hat{M}}{d\hat{t}} = -\hat{R}^2\hat{m} \tag{3}$$

where the non-dimensional variables are defined as $\hat{R}$=R/R_0, $\hat{t}$=t/τ, τ=$\sqrt{M_0/4\pi R_0 P_{abl}}$, $\hat{V} = V\tau/R_0$, $\hat{M} = M/M_0$, and $\hat{m} = \dot{m}(4\pi R_0^2/M_0)\hat{t}$. The mass ablation rate ($\dot{m}$) and ablation pressure (P_{abl}) are calculated using conservation of energy arguments by balancing the incoming laser intensity with the free-streaming heat flux. In this approximation, the

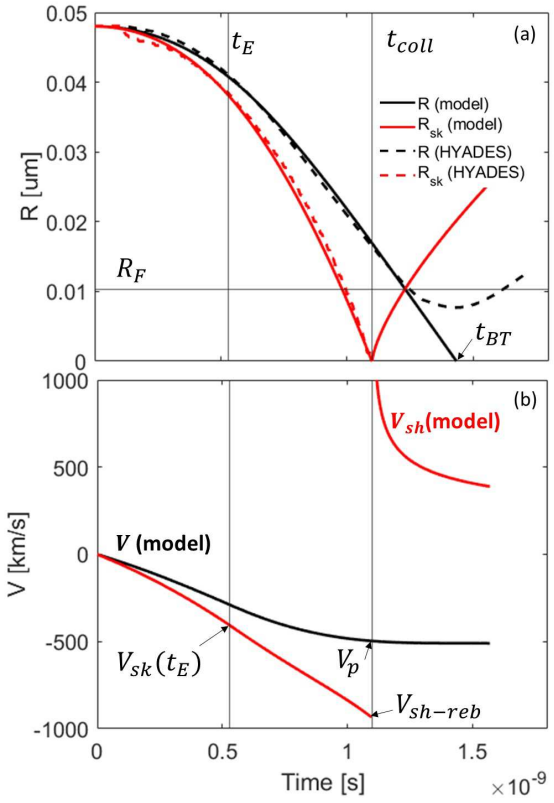

FIG. 2. Depiction of key variables in the exploding pusher model. (a) The shell trajectory (black) and shock trajectory (red) is shown as a function of time for the exploding pusher model, equations 1-7, (solid) and a HYADES simulation (dashed). The time where the linear shock phase ends, t_E, and the time of shock collapse (t_{coll}) as wells as the predicted final radius R_F where $R(t) = R_{sk}(t)$ are indicated using black horizontal and vertical lines. The bang-time of the model is also indicated when $R(t_{BT}) = 0$. (b) The shell (black) and shock (red) velocity are shown which are the time derivatives of the shell and shock trajectory from (a). Also indicated in the figure are the shock velocity at the end of the linear shock phase ($V_{sk}(t_E)$), the velocity of the shell at shock collapse (V_p) and the velocity of the shock right before it rebounds (V_{sh-red}). (a) and (b) illustrate the key variables used in the exploding pusher model to compute the hot-spot plasma conditions. Curves in red are for the shock trajectory and velocity, while curves in black are for the shell.

mass ablation is [31]

$$\dot{m} = 0.61 \frac{A_{shell}}{2Z_{shell}} I_{14}^{1/3} \ [\mathrm{g/cm^2/\mu s}], \tag{4}$$

and the ablation pressure is

$$P_{abl} = 24.7 \frac{A_{shell}}{2Z_{shell}} I_{14}^{2/3} [\mathrm{MBar}], \tag{5}$$

where the laser intensity I_{14} is the incident intensity on capsule in units of 10^{14} W/cm^2, A_{shell} is the averaged number of nucleons per ion, and Z_{shell} is the average ionic charge. The intensity is computed as

$$I = \beta \frac{E_L}{4\pi R_0^2 \Delta t}, \tag{6}$$

where β is a free parameter which will discussed when fitting the measurements. The intensity is assumed to be constant over the duration of the square laser pulse as the capsule implodes.

Equations 1-5 are solved using the initial capsule conditions, laser energy, and pulse duration. The density of the shell, ρ_{shell}, is assumed to be 2.3 g/cm^3 which is average for the glass production process and $A_{shell} = 19.8$ and $Z_{shell} = 9.9$. The evolution of the shell is used to compute the shock that traverses through the gas fill. From linear shock theory, the shock moves at a velocity 33% faster than the shell, i.e. $V_{sk} = (4/3)$V, when $\hat{R} \approx 1$ [3]. The evolution of the shock front accounting for the spherical geometry is determined by the differential equation given by

$$V_{sk} \equiv \frac{d\hat{R}_{sk}}{d\hat{t}} = -\frac{4}{3} \frac{\hat{V}}{\hat{R}^{1/3}} \ \{t < t_{coll}\}, \tag{7}$$

which applies until the shock front collapses to the center at time t_{coll}. The $1/\hat{R}^{1/3}$ factor captures the shock strengthening due to the spherical geometry, which only matters as the shock gets closer to the center of the sphere. Figure 2(a) displays the evolution of R and R_{sk} computed by the exploding pusher model (Equations 1-7) and with the radiation-hydrodynamics simulations HYADES [32]. Figure 2(a) depicts the trajectory of a 460 μm radius capsule with a 2.8 μm thick shell imploded with a laser energy of 7 kJ in a 0.6 ns pulse. The exploding pusher model was tuned to match the HYADES trajectory by varying the laser energy by a factor β=0.6. The HYADES simulations used a heat flux limiter of 0.04 to match the bang time. This is similar to an energy flux limiter. This demonstrates the exploding pusher model can capture the evolution of the shell and shock by tuning the energy absorbed by the capsule, which is also commonly done in most state-of-the-art simulations.

B. Linear Shock Phase

The shell equations of motion are used to compute the plasma conditions generated by the strong shock launched into the gas. Following the Rosen model [3], the linear shock phase ends at time, t_E, which occurs when the position of the shock is at

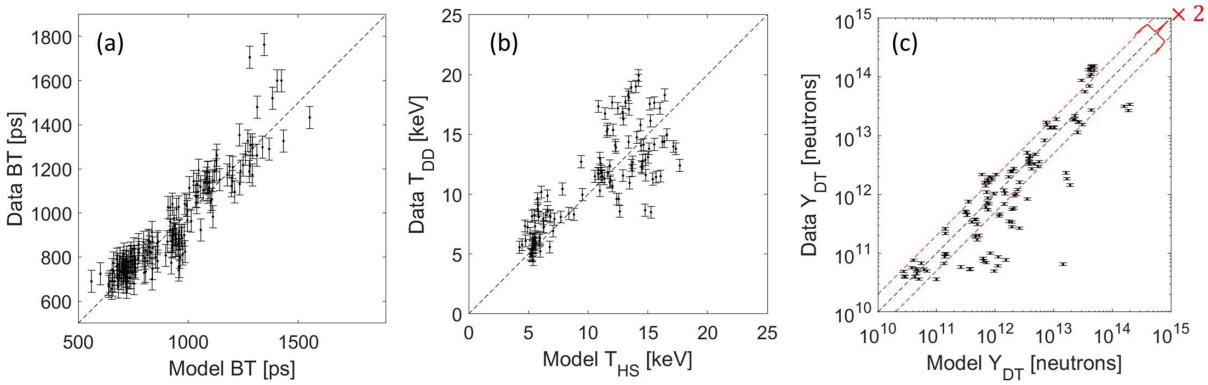

FIG. 3. Equations 1-7, 11, and 14-15 were solved using the initial conditions of each experiment to compute the shell and shock trajectory. Those trajectories were used to model t_{BT} (a), T_{HS} (b), and Y_{DT} (c) to compared to the DT data in the exploding pusher data base. An energy multiplier of 0.6 was use to calibrate the model t_{BT} to the data.

$\hat{R}_{sk}$=0.8. This coincides with half the mass of the gas being shocked. At this time a majority of the gas has been shocked at a radius large enough where the linear shock theory applies. The post-shock density (ρ_{ps}), ion temperature (T_{ps}), and pressure (P_{ps}) are given by the Rankine–Hugoniot relations for a strong shock in an ideal gas and are given by

$$\rho_{ps} = \frac{\gamma+1}{\gamma-1}\rho_0 \tag{8}$$

$$T_{ps} = \frac{3}{16}Am_pV_{sk}^2(t_E) \tag{9}$$

$$P_{ps} = \frac{Z+1}{Am_P}\rho_{ps}T_{ps}, \tag{10}$$

where $V_{sk}(t_E)$ is computed from Equation 7 and γ is the adiabatic index of the gas. In this situation $\gamma = 5/3$, but is kept general in the subsequent equations. The parameters A and Z are the average ion mass and ionic charge of the fuel computed from the fill fractions of the initial gas.

C. Adiabatic Compression Phase

The exploding pusher model in this work significantly deviates from Rosen in the calculation of the compression factor, η, which is defined as

$$\eta = \left(\frac{R_0}{R_F}\right)^3. \tag{11}$$

where R_F is the final radius reached by the shell before decompression. Rosen originally computed the compression solely on conservation of mass arguments. The method used an estimate for the fraction of shell mass remaining after ablation, combined with an approximation that the shell density profile would be $\rho_{shell}(r) = \rho(R_F)(R_F/r)^2$ at stagnation, which is motivated from the continuity equation. The final radius was calculated using conservation of mass and is given by

$$f_{abl}M_0 = 4\pi\int_{R_F}^{R_0}\rho_{shell}(r)r^2dr, \tag{12}$$

where f_{abl} is the fraction of shell mass remaining after ablation. In Rosen's work f_{abl} was assumed to be 1/2. Equation 12 is solved to express the compression in terms of the initial shell density, initial fuel density, capsule radius, and shell thickness, and is given by

$$\eta_{Rosen} = \left(1 + f_{abl}\frac{\rho_{shell}}{\rho_0}\frac{\Delta R}{R_0}\right)^3. \tag{13}$$

However, the compression prescribed in Equation 13 vastly overestimates the compression in exploding pushers, especially as the fill pressure decreases below 1.0 mg/cc.

Rosen's approximation assumes that the shell is hydro-dynamically compressing the gas, like a piston. The fundamental reason for the overestimation is the neglect of the physics governing the interaction of the gas and shell, which can truncate the compression before it reaches the ideal compression predicted by Rosen.

The hypothesis used in this work is that the inward motion of the shell is reversed by the return shock, well before the shell reaches peak compression. This implies that peak compression occurs at the radius at which the position of the shock intersects the position of the imploding shell, which can be written as

$$R(t^*) = R_{sk}(t^*) \equiv R_F, \tag{14}$$

where the time of this matching occurs at t^*. In order to compute R_F a model for the rebounding

shock is needed. A Guderly model for a spherically diverging shock is used [33]. The rebounding shock position is compute after t_{coll} as

$$R_{sk} = (V_{sk-reb} - V_p)(t - t_{coll})^{\alpha} \ \{t > t_{coll}\}, \quad (15)$$

where α is assumed to be 0.717, which is the analytic solution for a spherically diverging shock [33]. In the Guderly problem, the velocity of the rebounding shock is equivalent to the velocity of the converging shock, V_{sk-reb}. However, in this situation the rebounding shock is slowed by mass still converging inward at the shell velocity, V_p. A simple estimate for the tamping of the rebounding shock is to take the difference between the incident shock velocity and the pusher velocity at t_{coll}, i.e. the $(V_{sk-reb}-V_p)$ term in Eq. 15. Figure 2 (a) and (b) illustrates the definitions of R_F, V_{sk-reb}, and V_p.

Once the compression factor, η, has been computed using Equations 1-7, 11, and 14-15, the final plasma conditions are computed assuming adiabatic compression of the conditions at t_E. The hot-spot density, pressure, and temperature are computed as

$$\rho_{HS} = \eta\rho_0 \quad (16)$$

$$P_{HS} = P_{ps}\Big(\eta\frac{\gamma-1}{\gamma+1}\Big)^{5/3} \quad (17)$$

$$T_{HS} = \frac{Am_p}{Z+1}\frac{P_{HS}}{\rho_{HS}}. \quad (18)$$

The hot spot plasma conditions are subsequently used to compute the nuclear measurements.

D. Exploding Pusher Modeling of DT data

The main quantities of interest to model are the bang time (t_{BT}), hot spot temperature (T_{HS}) and neutron yield (Y_{DT}). All parameters are computed from the exploding pusher model presented above.

The bang time of the implosion is estimated by the convergence time of the free-falling shell, i.e. $R(t_{BT}) = 0$. Equations 1-7 were solved using the initial conditions for all 222 shots in the data base. The bang time predicted from the model was optimized by scaling the total energy absorbed by the capsule by a factor, β, which was determined to be β= 0.485±0.05 by minimizing the difference between the model prediction and the data. The measured bang time versus predicted is shown in Figure 3 (a). The computed R-squared indicates 84% of the variance is predictable by the model. The unaccounted for variance is within the uncertainty of the detector uncertainty of 50 ps. Scaling the laser energy deposited in the shell to calibrate the model's bang time constrains the energy balance which is important for computing the post-shock and hot-spot plasma conditions.

The temperature is directly computed from the hot spot pressure and density in Eq. 18. Figure 3 (b) displays the temperature data versus the modeled values. The exploding pusher model can account for 50% of the variance for the entire data set. However, the model appears to do better for experiments that produced hot spots with $T_{DT}<$ 10 keV, while the there exists a large variance when the implosions are driven to temperatures above 10 keV. Generally, implosions that produce the largest temperatures are low-fill density and high laser intensity. The source of the this variance is primarily due to unaccounted for physics in the exploding pusher model, which becomes important as the hot spot is driven to extreme states.

The yield is a challenging value to compute with simple models. The yields depends upon the details of the density and temperature evolution as well as profiles. The yield is computed form R_F, T_{HS}, and ρ_{HS} form the exploding pusher model and is given by

$$Y_{DT} = \frac{f_D f_T}{A^2 m_p^2}\rho_{HS}^2 \left\langle\sigma v\right\rangle_{DT} V_{HS}\tau_{burn}, \quad (19)$$

where $\tau_{burn} = R_F/c_S$, c_S is the sound speed, $V_{HS} = (4\pi/3)R_F^3$, and $\left\langle\sigma v\right\rangle_{DT}$ is the DT reactivity evaluated at T_{HS}. Figure 3(c) shows the comparison between the model and DT data. Remarkably, the models captures the yield scaling globally over the data set to with-in a factor of 2×. However, there is a high degree of variance that is unexplained. This is expected because the yields scales as $Y_{DT} \propto R_F^4 T_{HS}^{3.5}\rho_{HS}^2$ (assuming $\left\langle\sigma v\right\rangle_{DT} \propto T_{HS}^4$). The high powers of R_F, T_{HS}, and ρ_{HS} amplify any errors in the computed values. In addition, some experiments are systematically under-predicted, likely due to degradation effects not captured by the model. Some of the most discrepant yield measurements originate from shots conducted by Zylstra [27] and Sio [29] which utilized fuel fills containing trace amounts of deuterium or tritium. Accurately determining the atomic composition of the gas in these targets becomes increasingly challenging when fuel fractions fall below 1%. It is possible that uncertainties in the filling process introduce significant variations in fuel composition, thereby preventing the model from reliably predicting these yields.

One of the remarkable features of this model is its ability to reasonably capture the scaling of the data with two parameters, α and β. These controlled the rebounding shock trajectory and the mass ablation rate, respectively. The parameter β essential controls the energetics of the model and is used to optimize the bang time. The parameter α controls the compression of the shell. However, it was chosen *ad hoc* from analytic spherical shock theory.

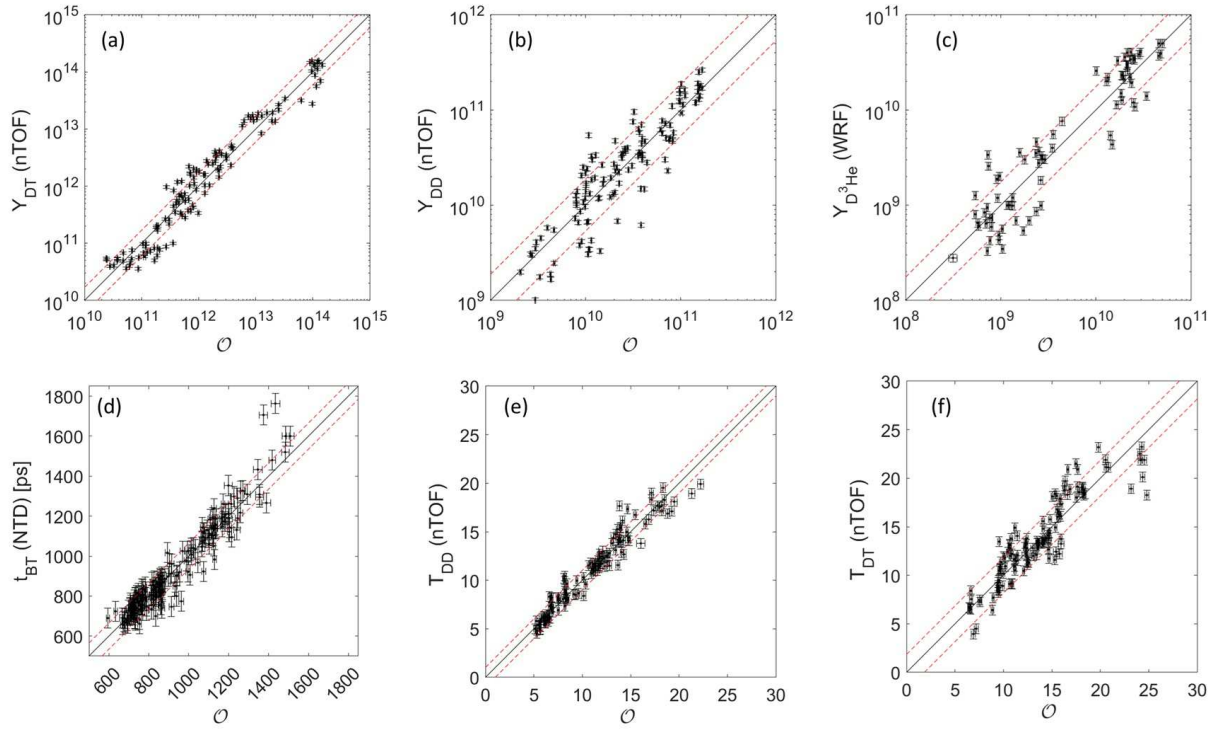

FIG. 4. Comparison between predicted quantities by Equation 23 and the measurements for Y_{DT} (a), Y_{DD} (b), Y_{D^3He} (c)), T_{DT} (d), T_{DD} (e), t_{BT} (f). Also shown is the 1-σ variance of the data compared to the model (dashed red lines).

E. Scaling Formulas

This section provides simple scaling laws for the three primary measurements predicted by the exploding pusher model. These equations are useful for gaining intuition and will later be used to motivate the functional form for direct fitting of the data set in Section IV.

The non-dimensional equations of motion of the shock and shell can help elucidate the scaling anticipated for the various measurements. The bang time of the implosion is exclusively proportional to $\hat{t}$ and the scaling is given by

$$t_{BT} \propto \hat{t} \propto \rho_{shell}^{1/2} \Delta R^{1/2} R_0^{7/3} E_L^{-1/3} \Delta t^{1/3}. \quad (20)$$

The hot-spot temperature depends upon the average ion mass, the shock velocity, and the compression and scales as $T_{HS} \propto \eta^{5/3} A V_{sk}^2(t_E)$. The equations governing the shock predict that the V_{sk} at time t_E scales inversely with $\hat{m}$ and $\hat{t}$ so long as $\hat{R} \gg 1$. In addition, the compression η is a approximately constant for the parameters encountered in this data set. These assumptions result in a scaling relation for the hot-spot temperature as

$$T_{HS} \propto \frac{A}{\hat{m}^2 \hat{t}^2} \propto \frac{A E_L^{2/3}}{R_0^{10/3} \Delta t^{2/3}}. \quad (21)$$

The DT yield scaling uses the scaling for T_{HS} and is

$$Y_{DT} \propto f_D f_T \rho_0^2 R_0^{4-10n/3} E_L^{2n/3} \Delta t^{-2n/3}, \quad (22)$$

where $\langle \sigma v \rangle_{DT} \propto (T_{HS})^n$ and n is the temperature dependent scaling power for the reactivity. For instance $n = 3.6$ for T_{HS} = 4-6 keV with 3% accuracy, but n=4.6 for 2-4 keV with 9% accuracy [34].

IV. EMPIRICAL SCALING FITS

The power-law scalings derived in the previous section motivate fitting generalized power-law formulas directly to the data to examine discrepancies between the predicted scaling and the theoretical scaling. In addition, these fits offer an efficient way to interpolate the data set and aid in the design of future experiments. For instance, experiments developing neutron source might wish to optimize the

$\mathcal{O}$	a	b	c	d	e	f	g	h	i	j
Y_{DT}	8.04×10^{13}	1.21	0.87	-0.04	1.00	-1.93	4.30	1.0	-1.52	-0.34
Y_{DD}	3.16×10^{11}	1.02	2.43	0.08	0.03	0.15	0.78	1.07	-0.56	-0.01
Y_{D3He}	1.24×10^{11}	0.23	0.80	0.84	-0.02	-1.19	2.84	2.34	-2.47	0.46
T_{DT}	8.83	-0.26	-0.02	0.01	0.02	-0.27	-0.19	0.29	-0.58	-0.09
T_{DD}	9.17	-0.20	-0.09	-0.02	0.01	1.51	-0.21	0.73	-0.58	0.05
t_{BT}	1010	0.01	0.00	0.00	0.0	0.40	0.56	-0.28	0.46	0.02

TABLE I. Summary of the exponents that minimize the variance between Equations 23 and the data.

DT or DD yield while experiments studying low-cross-section nuclear reaction might maximize the hot spot temperature and volume.

The measurements are fit to a generic power-law scaling formula, $\mathcal{O}$, given by:

$$\mathcal{O} = a\Big(\frac{\rho}{3g/cc}\Big)^{b}\Big(f_D\Big)^{c}\Big(f_{3He}\Big)^{d}\Big(f_T\Big)^{e}\Big(\frac{R_0}{430\mu m}\Big)^{f}\Big(\frac{\Delta R}{3\mu m}\Big)^{g}\Big(\frac{E_L}{20kJ}\Big)^{h}\Big(\frac{\Delta t}{1ns}\Big)^{i}\Big(\frac{1-\delta R}{1\mu m}\Big)^{j}, \tag{23}$$

where a through j are free parameters constrained by the data. The free parameters are optimized by a least squares regression that minimizes the difference between the data and the prediction made by Equation 23.

Figure 4 displays the data versus modeled values using Equation 23. The fitted exponents are displayed in Table I. Figure 4(d) shows the fitting to the measured bang time, which found that $t_{BT} \propto \Delta R^{0.56} {R_0}^{0.40} E_L^{-0.28} \Delta t^{0.46}$, which is similar to the scaling predicted by Equation 20, however, there is notable difference in the scaling of the bang time with R_0. The data indicates a much weaker dependence on the capsule size which implies that more of the laser energy is coupled to larger capsules. Recent direct-drive experiments both at NIF and OMEGA also observed increased energy coupling based upon the capsule size, beam size, and average intensity on capsule [35, 36]. These previous results suggest that as R_0 increases the ratio of the beam size to target diminishes which increases the hydrodynamic efficiency of the implosion by mitigating various laser-plasma instabilities. This leads to faster implosion velocities, which cause the earlier bang-times in this data set.

The inferred scaling for the nuclear yields and ion temperatures are much more difficult to interpret because multiple effects are simultaneously impacting the data. The dominant terms for the DT and DD temperature are $T_{DT} \propto \rho^{-0.26} \Delta R^{-0.19} {R_0}^{-0.27} E_L^{0.29} \Delta t^{-0.58}$ and $T_{DD} \propto \rho^{-0.20} \Delta R^{-0.21} {R_0}^{1.51} E_L^{0.73} \Delta t^{-0.58}$, which should be compared with Eq. 21. For T_{DT} and T_{DD} the most notable deviations in scaling are observed with ρ_0, R_0, and ΔR. The data indicate that the temperature depends on ρ and scales either weakly or proportionally to R_0. These observations suggest that the temperature has a dependency on η, which is a function of both ρ_0, R_0, and ΔR. However, the exploding pusher model predicted negligible variations in η in this data set. X-ray imaging to measure the compression of these implosions has been studied, however, the results suggest the x-ray images are sensitive to the mixing of the shell and fuel rather than the convergence [16]. The probable cause of the deviations of the experimental scaling of T_{DD} and T_{DT} is due to kinetic effects which modify how the shock couples energy to the gas [37, 38]. Another, issue is that both T_{DD} and T_{DT} are impacted by flows in the hot spot [39]. It is unclear how flows in the hot spot impact the scaling observed.

The fitted scaling for Y_{DT}, Y_{DD}, and Y_{D3He} can only reproduce the measured yields to at best a factor of 2× across the data set. One source of error could be that the yield depends upon the fusion reactivity which is a nonlinear function of the ion temperature. As noted in Equation 22 the power law exponents are indeed functions of the hot spot temperature. In addition, the yield is a complex function of different physics governing the densities and temperatures of the implosion that are not modeled here. However, the yield scaling provided here are immensely useful for providing predictions when setting up diagnostics because a factor of 2× is generally acceptable on the dynamic range of most instruments at OMEGA.

Furthermore, it is interesting to examine the dataset's inference of yield scaling with fill composition. Several studies have observed anomalous yield scaling by adding different elements to the main fuel [40–43]. Specifically, there has been consider-

able study of yield scaling with the addition of ^{3}He to a pure D_2 fuel. The empirical model suggests that $Y_{DD} \propto f_D^{2.43} f_{^3He}^{0.08} f_T^{0.03}$, which agrees with previous studies that there is an anomalous degradation of DD yields as ^{3}He and T are added to the fuel. In addition, Casey observed degradation in the scaling Y_{DD}/Y_{DT} which is expected to scale as f_D/f_T. This work inferred $Y_{DD}/Y_{DT} \propto f_D^{1.56}/f_T^{0.92}$, which also degrades this ratio if $f_T = 1 - f_D$. However, it should be noted that the scaling observed in the data set predict much weaker yield degradations than observed in the focused experiments. This is likely due to these anomalous effects competing with other degradation mechanisms across the 222 experiments.

V. YIELD DEGRADATION AS A FUNCTION OF ρ_0

A large topic of research pertains to the observed degradation of nuclear yields as a function of ρ_0 [15, 16, 29, 44, 45]. Experiments have observed a substantial drop off in yield as ρ_0 decreases, which has been attributed to Knudsen effects [21]. In contrast, radiation hydrodynamics codes predict the nuclear yield has a weak scaling with ρ_0 [16, 21, 46], and a number of models including kinetic effects must be included to capture the yield degradation [47]. The primary reason for the discrepancy is that radiation-hydrodynamics codes over predict the compression of the capsule at lower initial densities, holding all other variables constant. The increase in compression increases ρ_{HS} and T_{HS} through pdV work which maintains the yield even though the total number of atoms in the gas decreases.

The model presented in Section III truncates the compression by hypothesizing that the return shock has enough momentum to modify the trajectory of the incoming shell. Generally, this model predicts η to be approximately constant for the implosions in the data base and is generally limited to convergence ratios of ≈4. This preserves the yield scaling proportional to the initial fill density, which is more consistent with experiments. However, the key reason attributed to the anomalous yield scaling is the fact that the average mean free path of ions in the hot spot of exploding pushes gets too large to be accurately simulated by radiation hydrodynamics codes [15, 47]. While the exploding pusher model presented in this work completely neglects this physics, it helps elucidate the key problem lies with modeling the shell's compression of the gas.

The database presented has a wide range of experiments to test kinetic implosions models to capture the yield trends observed in the data. For instance, the data set suggests the scaling of yield with ρ_0 is reaction dependent. Figure 5 illustrates this dependence by plotting the measured yield for the DT, DD, and D^{3}He reaction normalized to power-law model without ρ_0 dependence ($\mathcal{O}(\rho_0)$). The DT and DD yield show a comparable sensitivity to ρ_0, while the D^{3}He yield is much less sensitive over similar densities.

VI. CONCLUSIONS AND FUTURE WORK

A large data base of exploding-pusher implosions was presented and offers a catalogue of experiments that are useful for diagnostic development, studying stellar nucleosynthesis, and generating neutron sources. Empirical scaling formulas were provided for efficient interpolation of the data set. These formulas are useful in estimating bang times and yields for setting up diagnostics in future experiments. The data base can be used as a base line to compare the performance of new experiments.

In addition, a simplified model of an exploding pusher was presented and was shown to reasonably capture trends observed in the data set. The model could be used to predict the performance of glass shell implosions when the initial conditions are outside the current data set. However, there is a high degree of variance due to the missing physics of the reduced model.

In the future, the database will be expanded to include more experiments with different shell materials. New measurements will also be added, such as data collected with x-ray imaging and x-ray spectroscopy. Furthermore, the large data set presented here opens new opportunities for large-scale data analysis. As mentioned previously, a large effort has been expended to study the physics missing in radiation hydrodynamics codes as hot spot transitions into the kinetic regime. This data set can be used to test models for these kinetic effects over a wide array of parameters. The data set also enables quantifying shot-to-shot variations, which has been historically difficult to do in ICF.

VII. SUPPLEMENTARY MATERIAL

The data for all experiments presented in this paper are available in the supplementary material as an excel file. This data is as accurate as possible. The values for capsule conditions are taken from target meteorology provided by General Atomics. The values for the nuclear data are taken from official values reported in the OMEGA data base. The laser characteristics are taken from the as-shot characterization of the performance.

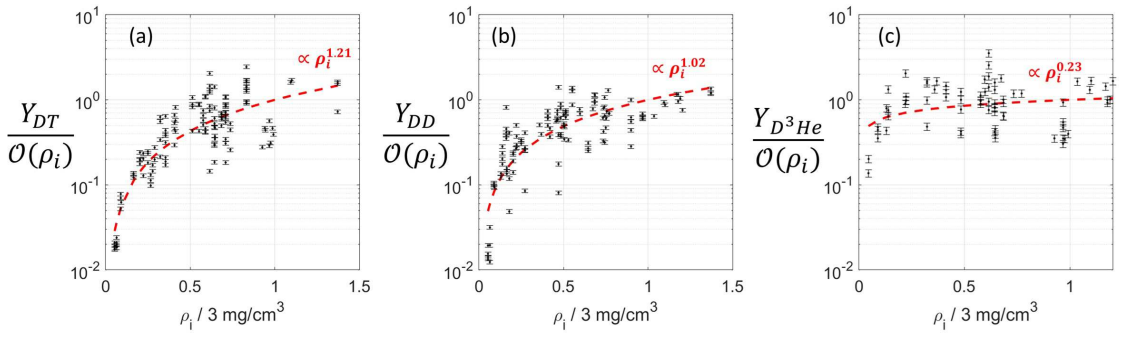

FIG. 5. Measured Y_{DT} (a), Y_{DD} (b), Y_{D^3He} (c) normalized to the model predictions $\mathcal{O}$ as a function of ρ_0. Also shown is the scaling proportional to ρ_0 found from the model fitting (dashed red lines).

ACKNOWLEDGMENTS

This work was performed under the auspices of the U.S. Department of Energy by LANL under Contract No. DE-AC52–06NA25396. P.J.A. was supported by Grant No. DE-NA0003960.

This material is based upon work supported by the Department of Energy National Nuclear Security Administration under Award No. DE-NA0003856, DE-NA0003525, and DE-NA0003868. And by the Office of Science under DE-FG02- 88ER40387.

The experiments were conducted at the Omega Laser Facility with the beam time through the Laboratory Basic Science and National Laser User Facility allocation through the Department of Energy under Contract No. DE-NA0003856, DE-NA0002035, DE-NA0001857, DE-NA0002949, DE-NA0002905, DE-NA0001857, DE-FC52-08NA28752, DE-NA0002035

The experiments were also supported by LLE under contract No. 417532G/UR FAO GR510907 and No. 415935-G. And by Lawrence Livermore National Laboratory under contract No. B597367.

The authors thank the OMEGA operations crew for executing these experiments, and Ernie Doeg and Robert Frankel for processing of the CR-39 data used in this work. We also thank M. Rosenberg, O. Mannion and B. Aguirre for conducting and sharing experiments that comprise this data set.

This report was prepared as an account of work sponsored by an agency of the United States Government. Neither the United States Government nor any agency thereof, nor any of their employees, makes any warranty, express or implied, or assumes any legal liability or responsibility for the accuracy, completeness, or usefulness of any information, apparatus, product, or process disclosed, or represents that its use would not infringe privately owned rights. Reference herein to any specific commercial product, process, or service by trade name, trademark, manufacturer, or otherwise does not necessarily constitute or imply its endorsement, recommendation, or favoring by the United States Government or any agency thereof. The views and opinions of authors expressed herein do not necessarily state or reflect those of the United States Government or any agency thereof.

DATA AVAILABILITY STATEMENT

The data that support the findings of this study are available from the corresponding author upon reasonable request.

[1] T. R. Boehly, D. L. Brown, R. S. Craxton, R. L. Keck, J. P. Knauer, J. H. Kelly, T. J. Kessler, S. A. Kumpan, S. J. Loucks, S. A. Letzring, F. J. Marshall, R. L. McCrory, S. F. B. Morse, W. Seka, J. M. Soures, and C. P. Verdon, Optics Communications **133**, 495 (1997).

[2] G. H. Miller, E. I. Moses, and C. R. Wuest, Optical Engineering **43** (2004), 10.1117/1.1814767, institution: Lawrence Livermore National Lab. (LLNL), Livermore, CA (United States) Number: UCRL-JRNL-204517.

[3] M. D. Rosen and J. H. Nuckolls, Physics of Fluids **22**, 1393 (1979).

[4] S. Le Pape, L. Divol, L. Berzak Hopkins, A. Mackinnon, N. Meezan, D. Casey, J. Frenje, H. Herrmann, J. McNaney, T. Ma, K. Widmann, A. Pak, G. Grimm, J. Knauer, R. Petrasso, A. Zylstra, H. Rinderknecht, M. Rosenberg, M. Gatu-Johnson,

and J. Kilkenny, **112**, 225002.
[5] D. L. Bleuel, C. B. Yeamans, L. A. Bernstein, R. M. Bionta, J. A. Caggiano, D. T. Casey, G. W. Cooper, O. B. Drury, J. A. Frenje, C. A. Hagmann, R. Hatarik, J. P. Knauer, M. G. Johnson, K. M. Knittel, R. J. Leeper, J. M. McNaney, M. Moran, C. L. Ruiz, and D. H. G. Schneider, Review of Scientific Instruments **83**, 10D313 (2012).
[6] C. B. Yeamans and D. L. Bleuel, **72**, 120.
[7] A. Mackinnon, S. Lepape, R. Wallace, M. Schneider, K. Lafortune, P. McKenty, S. Craxton, R. Janezic, W. Shmayda, C. Sangster, A. Nikroo, and M. Hoppe, (2010).
[8] C. Yeamans, G. Kemp, Z. Walters, H. Whitley, P. McKenty, E. Garcia, Y. Yang, R. Craxton, and B. Blue, **61**, 046031.
[9] M. Hohenberger, S. Kerr, C. Yeamans, D. Rusby, K. D. Meaney, K. Hahn, R. Heredia, T. Sarginson, B. Blue, A. J. Mackinnon, and W. W. Hsing, **93**, 103510.
[10] M. Gatu Johnson, A. B. Zylstra, A. Bacher, C. R. Brune, D. T. Casey, C. Forrest, H. W. Herrmann, M. Hohenberger, D. B. Sayre, R. M. Bionta, J.-L. Bourgade, J. A. Caggiano, C. Cerjan, R. S. Craxton, D. Dearborn, M. Farrell, J. A. Frenje, E. M. Garcia, V. Y. Glebov, G. Hale, E. P. Hartouni, R. Hatarik, M. Hohensee, D. M. Holunga, M. Hoppe, R. Janezic, S. F. Khan, J. D. Kilkenny, Y. H. Kim, J. P. Knauer, T. R. Kohut, B. Lahmann, O. Landoas, C. K. Li, F. J. Marshall, L. Masse, A. McEvoy, P. McKenty, D. P. McNabb, A. Nikroo, T. G. Parham, M. Paris, R. D. Petrasso, J. Pino, P. B. Radha, B. Remington, H. G. Rinderknecht, H. Robey, M. J. Rosenberg, B. Rosse, M. Rubery, T. C. Sangster, J. Sanchez, M. Schmitt, M. Schoff, F. H. Séguin, W. Seka, H. Sio, C. Stoeckl, and R. E. Tipton, Physics of Plasmas **24**, 041407 (2017).
[11] A. Zylstra, J. Frenje, M. Gatu Johnson, G. Hale, C. Brune, A. Bacher, D. Casey, C. Li, D. McNabb, M. Paris, R. Petrasso, T. Sangster, D. Sayre, and F. Séguin, Physical Review Letters **119**, 222701 (2017), publisher: American Physical Society.
[12] P. J. Adrian, B. Bachmann, D. T. Casey, R. S. Craxton, W. Garbett, M. G. Johnson, E. Hartouni, M. Hohenberger, D. Holunga, N. V. Kabadi, S. Khan, J. Kunimune, B. Lahmann, G. D. Sutcliffe, H. D. Whitley, A. Zylstra, and J. A. Frenje, Physics of Plasmas **32**, 022704 (2025).
[13] J. Frenje, R. Florido, R. Mancini, T. Nagayama, P. Grabowski, H. Rinderknecht, H. Sio, A. Zylstra, M. Gatu Johnson, C. Li, F. Séguin, R. Petrasso, V. Y. Glebov, and S. Regan, Physical Review Letters **122**, 015002 (2019).
[14] P. J. Adrian, R. Florido, P. E. Grabowski, R. Mancini, B. Bachmann, L. X. Benedict, M. G. Johnson, N. Kabadi, B. Lahmann, C. K. Li, R. D. Petrasso, H. G. Rinderknecht, S. P. Regan, F. H. Séguin, R. L. Singleton, H. Sio, G. D. Sutcliffe, H. D. Whitley, and J. A. Frenje, Physical Review E **106**, L053201 (2022).
[15] M. Rosenberg, H. Rinderknecht, N. Hoffman, P. Amendt, S. Atzeni, A. Zylstra, C. Li, F. Séguin, H. Sio, M. G. Johnson, J. Frenje, R. Petrasso, V. Glebov, C. Stoeckl, W. Seka, F. Marshall, J. Delettrez, T. Sangster, R. Betti, V. Goncharov, D. Meyerhofer, S. Skupsky, C. Bellei, J. Pino, S. Wilks, G. Kagan, K. Molvig, and A. Nikroo, Physical Review Letters **112**, 185001 (2014).
[16] H. Sio, O. Larroche, A. Bose, S. Atzeni, J. A. Frenje, N. V. Kabadi, M. Gatu Johnson, C. K. Li, V. Glebov, C. Stoeckl, B. Lahmann, P. J. Adrian, S. P. Regan, A. Birkel, F. H. Seguin, and R. D. Petrasso, Physics of Plasmas **29**, 072710 (2022).
[17] H. Rinderknecht, H. Sio, C. Li, A. Zylstra, M. Rosenberg, P. Amendt, J. Delettrez, C. Bellei, J. Frenje, M. Gatu Johnson, F. Séguin, R. Petrasso, R. Betti, V. Y. Glebov, D. Meyerhofer, T. Sangster, C. Stoeckl, O. Landen, V. Smalyuk, S. Wilks, A. Greenwood, and A. Nikroo, Physical Review Letters **112**, 135001 (2014).
[18] O. Mannion, J. Knauer, V. Glebov, C. Forrest, A. Liu, Z. Mohamed, M. Romanofsky, T. Sangster, C. Stoeckl, and S. Regan, Nuclear Instruments and Methods in Physics Research Section A: Accelerators, Spectrometers, Detectors and Associated Equipment **964**, 163774 (2020).
[19] F. H. Séguin, J. A. Frenje, C. K. Li, D. G. Hicks, S. Kurebayashi, J. R. Rygg, B.-E. Schwartz, R. D. Petrasso, S. Roberts, J. M. Soures, D. D. Meyerhofer, T. C. Sangster, J. P. Knauer, C. Sorce, V. Y. Glebov, C. Stoeckl, T. W. Phillips, R. J. Leeper, K. Fletcher, and S. Padalino, Review of Scientific Instruments **74**, 975 (2003).
[20] C. Stoeckl, R. Boni, F. Ehrne, C. J. Forrest, V. Y. Glebov, J. Katz, D. J. Lonobile, J. Magoon, S. P. Regan, M. J. Shoup, A. Sorce, C. Sorce, T. C. Sangster, and D. Weiner, Review of Scientific Instruments **87**, 053501 (2016).
[21] M. J. Rosenberg, F. H. Séguin, P. A. Amendt, S. Atzeni, H. G. Rinderknecht, N. M. Hoffman, A. B. Zylstra, C. K. Li, H. Sio, M. Gatu Johnson, J. A. Frenje, R. D. Petrasso, V. Y. Glebov, C. Stoeckl, W. Seka, F. J. Marshall, J. A. Delettrez, T. C. Sangster, R. Betti, S. C. Wilks, J. Pino, G. Kagan, K. Molvig, and A. Nikroo, Physics of Plasmas **22**, 062702 (2015).
[22] H. G. Rinderknecht, M. Rosenberg, C. Li, N. Hoffman, G. Kagan, A. Zylstra, H. Sio, J. Frenje, M. Gatu Johnson, F. Séguin, R. Petrasso, P. Amendt, C. Bellei, S. Wilks, J. Delettrez, V. Glebov, C. Stoeckl, T. Sangster, D. Meyerhofer, and A. Nikroo, Physical Review Letters **114**, 025001 (2015).
[23] N. V. Kabadi, R. Simpson, P. J. Adrian, A. Bose, J. A. Frenje, M. Gatu Johnson, B. Lahmann, C. K. Li, C. E. Parker, F. H. Séguin, G. D. Sutcliffe, R. D. Petrasso, S. Atzeni, J. Eriksson, C. Forrest, S. Fess, V. Y. Glebov, R. Janezic, O. M. Mannion, H. G. Rinderknecht, M. J. Rosenberg, C. Stoeckl, G. Kagan, M. Hoppe, R. Luo, M. Schoff, C. Shuldberg, H. W. Sio, J. Sanchez, L. B. Hopkins, D. Schloss-

berg, K. Hahn, and C. Yeamans, Physical Review E **104**, L013201 (2021).
[24] O. M. Mannion, W. T. Taitano, B. D. Appelbe, A. J. Crilly, C. J. Forrest, V. Y. Glebov, J. P. Knauer, P. W. McKenty, Z. L. Mohamed, C. Stoeckl, B. D. Keenan, J. P. Chittenden, P. Adrian, J. Frenje, N. Kabadi, M. Gatu Johnson, and S. P. Regan, **108**, 035201.
[25] B. Aguirre, "Sandia national laboratories FY21 progress report,".
[26] M. Gatu Johnson, C. Forrest, D. Sayre, A. Bacher, J.-L. Bourgade, C. Brune, J. Caggiano, D. Casey, J. Frenje, V. Glebov, G. Hale, R. Hatarik, H. Herrmann, R. Janezic, Y. Kim, J. Knauer, O. Landoas, D. McNabb, M. Paris, R. Petrasso, J. Pino, S. Quaglioni, B. Rosse, J. Sanchez, T. Sangster, H. Sio, W. Shmayda, C. Stoeckl, I. Thompson, and A. Zylstra, **121**, 042501.
[27] A. Zylstra, H. Herrmann, M. G. Johnson, Y. Kim, J. Frenje, G. Hale, C. Li, M. Rubery, M. Paris, A. Bacher, C. Brune, C. Forrest, V. Glebov, R. Janezic, D. McNabb, A. Nikroo, J. Pino, T. Sangster, F. Séguin, W. Seka, H. Sio, C. Stoeckl, and R. Petrasso, Physical Review Letters **117**, 035002 (2016).
[28] G. Sutcliffe, P. Adrian, J. Pearcy, T. Johnson, N. Kabadi, S. Haque, C. Parker, B. Lahmann, J. Frenje, M. Gatu-Johnson, H. Sio, F. Séguin, B. Pollock, J. Moody, V. Glebov, R. Janezic, M. Koch, R. Petrasso, and C. Li, Review of Scientific Instruments **92**, 063524 (2021).
[29] H. Sio, J. Frenje, A. Le, S. Atzeni, T. Kwan, M. Gatu Johnson, G. Kagan, C. Stoeckl, C. Li, C. Parker, C. Forrest, V. Glebov, N. Kabadi, A. Bose, H. Rinderknecht, P. Amendt, D. Casey, R. Mancini, W. Taitano, B. Keenan, A. Simakov, L. Chacón, S. Regan, T. Sangster, E. Campbell, F. Seguin, and R. Petrasso, Physical Review Letters **122**, 035001 (2019).
[30] H. Sio, O. Larroche, S. Atzeni, N. V. Kabadi, J. A. Frenje, M. Gatu Johnson, C. Stoeckl, C. K. Li, C. J. Forrest, V. Glebov, P. J. Adrian, A. Bose, A. Birkel, S. P. Regan, F. H. Seguin, and R. D. Petrasso, Physics of Plasmas **26**, 072703 (2019).
[31] B. Scheiner and M. Schmitt, Physics of Plasmas **26**, 024502 (2019).
[32] J. T. Larsen and S. M. Lane, Journal of Quantitative Spectroscopy and Radiative Transfer Special Issue Radiative Properties of Hot Dense Matter, **51**, 179 (1994).
[33] J. J. Ruby, J. R. Rygg, J. A. Gaffney, B. Bachmann, and G. W. Collins, Physics of Fluids **31**, 126104 (2019).
[34] D. T. Casey, D. B. Sayre, C. R. Brune, V. A. Smalyuk, C. R. Weber, R. E. Tipton, J. E. Pino, G. P. Grim, B. A. Remington, D. Dearborn, L. R. Benedetti, J. A. Frenje, M. Gatu-Johnson, R. Hatarik, N. Izumi, J. M. McNaney, T. Ma, G. A. Kyrala, S. MacLaren, J. Salmonson, S. F. Khan, A. Pak, L. B. Hopkins, S. LePape, B. K. Spears, N. B. Meezan, L. Divol, C. B. Yeamans, J. A. Caggiano, D. P. McNabb, D. M. Holunga, M. Chiarappa-Zucca, T. R. Kohut, and T. G. Parham, Nature Physics **13**, 1227 (2017), number: 12 Publisher: Nature Publishing Group.
[35] D. H. Froula, I. V. Igumenshchev, D. T. Michel, D. H. Edgell, R. Follett, V. Y. Glebov, V. N. Goncharov, J. Kwiatkowski, F. J. Marshall, P. B. Radha, W. Seka, C. Sorce, S. Stagnitto, C. Stoeckl, and T. C. Sangster, **108**, 125003.
[36] N. S. Krasheninnikova, M. J. Schmitt, K. Molvig, S. C. Hsu, B. S. Scheiner, D. W. Schmidt, V. Geppert-Kleinrath, P. W. McKenty, D. T. Michel, D. H. Edgell, F. J. Marshall, and H. Huang, **27**, 022706.
[37] W. T. Taitano, A. N. Simakov, L. Chacón, and B. Keenan, Physics of Plasmas **25**, 056310 (2018).
[38] O. Larroche, H. G. Rinderknecht, M. J. Rosenberg, N. M. Hoffman, S. Atzeni, R. D. Petrasso, P. A. Amendt, and F. H. Séguin, Physics of Plasmas **23**, 012701 (2016).
[39] M. Gatu Johnson, D. T. Casey, J. A. Frenje, C.-K. Li, F. H. Séguin, R. D. Petrasso, R. Ashabranner, R. Bionta, S. LePape, M. McKernan, A. Mackinnon, J. D. Kilkenny, J. Knauer, and T. C. Sangster, Physics of Plasmas **20**, 042707 (2013).
[40] J. R. Rygg, J. A. Frenje, C. K. Li, F. H. Séguin, R. D. Petrasso, J. A. Delettrez, V. Y. Glebov, V. N. Goncharov, D. D. Meyerhofer, S. P. Regan, T. C. Sangster, and C. Stoeckl, Physics of Plasmas **13**, 052702 (2006), publisher: American Institute of Physics.
[41] H. W. Herrmann, J. R. Langenbrunner, J. M. Mack, J. H. Cooley, D. C. Wilson, S. C. Evans, T. J. Sedillo, G. A. Kyrala, S. E. Caldwell, C. S. Young, A. Nobile, J. Wermer, S. Paglieri, A. M. McEvoy, Y. Kim, S. H. Batha, C. J. Horsfield, D. Drew, W. Garbett, M. Rubery, V. Y. Glebov, S. Roberts, and J. A. Frenje, Physics of Plasmas **16**, 056312 (2009), publisher: American Institute of Physics.
[42] Y. Kim, H. W. Herrmann, N. M. Hoffman, M. J. Schmitt, G. Kagan, A. M. McEvoy, A. B. Zylstra, J. M. Smidt, S. Gales, A. Leatherland, M. Rubery, M. Gatu Johnson, J. A. Frenje, V. Yu Glebov, and C. Forrest, Physics of Plasmas **28**, 012707 (2021).
[43] D. T. Casey, J. A. Frenje, M. Gatu Johnson, M. J.-E. Manuel, H. G. Rinderknecht, N. Sinenian, F. H. Séguin, C. K. Li, R. D. Petrasso, P. B. Radha, J. A. Delettrez, V. Y. Glebov, D. D. Meyerhofer, T. C. Sangster, D. P. McNabb, P. A. Amendt, R. N. Boyd, J. R. Rygg, H. W. Herrmann, Y. H. Kim, and A. D. Bacher, Physical Review Letters **108**, 075002 (2012).
[44] H. G. Rinderknecht, H. Sio, C. K. Li, N. Hoffman, A. B. Zylstra, M. J. Rosenberg, J. A. Frenje, M. Gatu Johnson, F. H. Séguin, R. D. Petrasso, R. Betti, V. Yu Glebov, D. D. Meyerhofer, T. C. Sangster, W. Seka, C. Stoeckl, G. Kagan, K. Molvig, C. Bellei, P. Amendt, O. Landen, J. R. Rygg, V. A. Smalyuk, S. Wilks, A. Greenwood, and A. Nikroo, Physics of Plasmas **21**, 056311 (2014).

[45] H. G. Rinderknecht, P. A. Amendt, S. C. Wilks, and G. Collins, Plasma Physics and Controlled Fusion **60**, 064001 (2018), publisher: IOP Publishing.

[46] N. Kabadi, en*Exploring evolution of multi-ion effects and electron temperature in ICF implosions at Omega and the NIF*, Thesis, Massachusetts Institute of Technology (2022), accepted: 2022-06-15T13:11:20Z.

[47] N. M. Hoffman, G. B. Zimmerman, K. Molvig, H. G. Rinderknecht, M. J. Rosenberg, B. J. Albright, A. N. Simakov, H. Sio, A. B. Zylstra, M. Gatu Johnson, F. H. Séguin, J. A. Frenje, C. K. Li, R. D. Petrasso, D. M. Higdon, G. Srinivasan, V. Y. Glebov, C. Stoeckl, W. Seka, and T. C. Sangster, Physics of Plasmas **22**, 052707 (2015).